AIAA JOURNAL
Vol. 35, No. 5, May 1997

Coupled Fluid-Structural Characteristics of Actuators for Flow Control

Ruben Rathnasingham* and Kenneth S. Breuer†
Massachusetts Institute of Technology, Cambridge, Massachusetts 02139

The characteristics of a typical flow control actuator design are discussed. The device is based on a resonating structure that interacts with a closed volume of fluid to create a concentrated jet through an exit orifice. The resulting unsteady flow through the orifice introduces viscous effects that are characterized by the Stokes parameter based on the orifice diameter. An optimum operating Stokes parameter is then computed by matching this viscous dominated solution to an ideal, inviscid result. The actuator is modeled with a system of coupled equations that describe its fluid-structural behavior. This model is compared to experimental results and is seen to predict time and frequency characteristics well. Experimental data also show that, away from the exit orifice, the jet is self-similar and its intensity is also governed by the Stokes parameter.

Nomenclature

A = membrane area, m^2
a = hole area, m^2
C_0 = structural damping, Ns/m
D = membrane diameter, m
d = hole diameter, m
E = material Young's modulus, N/m^2
G_0 = forcing amplitude, N
H = cavity height, m
I_0 = mass moment of inertia, kg-m^2
K_0 = spring stiffness, N/m
l_S = Stokes length scale $\sqrt{(\nu/\omega)}$, m
M = membrane mass, kg
M_a = mass per unit area, kg/m^2
P = instantaneous pressure, N/m^2
P_0 = ambient pressure, N/m^2
Q = quality factor
R = universal gas constant, Nm/kg K
r = radial distance from the membrane centroid, m
T = fluid temperature, K
t = membrane thickness, m
t_c = cap thickness (orifice depth) for the membrane device, m
u = mean jet velocity, m/s
x = normalized membrane displacement
θ = angle about the membrane centroid
ν = fluid kinematic viscosity, m^2/s
ν_p = Poisson's ratio
Π_x = pressure gradient in the flow direction, N/m^3
ρ = fluid density, kg/m^3

I. Introduction

INTEREST in active flow control for drag or noise reduction, flow vectoring, etc.,[1–5] has stimulated the recent development of innovative actuator designs that create localized disturbances in a flowfield. A family of such actuators utilizes the large displacements attainable when structural members are driven at their resonant frequencies. These resonating structures are used to create pressure fluctuations in a closed cavity with an opening through which fluid is driven and used as a control input. Because of the relatively small sizes and high natural frequencies of the devices, off-resonance forcing will not provide sufficient deflections for control.

One such design, referred to here as the membrane actuator, is illustrated schematically in Fig. 1a. First proposed by Coe et al.,[6] it consists of a thin membrane rigidly fixed at its edges and driven into transverse oscillations at its resonant frequency. The membrane makes up an end wall of a closed, cylindrical cavity. The opposite wall is rigid and contains a small orifice. As the membrane deflects to compress the fluid in the cavity, the increase in pressure drives fluid out through the orifice. This outflow separates at the edge of the orifice and emerges as a normal jet. When the membrane deflects in the opposite direction, the orifice acts as a sink and fluid is drawn into the cavity from all directions. The differences between the inflow and outflow result in a time-averaged flowfield resembling a vortex ring over the orifice with a steady jet emanating outward from its core. Coe et al.[6] fabricated a micromachined actuator with orifice diameters of 150 to 300 μm that achieved jet velocities of 17 m/s and penetration depths of 500 orifice diameters. Similar devices were also used to achieve jet thrust vectoring. An experimental investigation of the turbulent jet produced by a similar macrosized device has also been carried out by James et al.[7]

A second design, referred to here as the springboard actuator, was first proposed by Jacobson and Reynolds[3] and comprises a piezoceramic/metal shim heterogeneous bimorph cantilever mounted eccentrically over an open cavity (Fig. 1b). The cantilever is driven at resonance and the oscillatory cavity pressure created, in turn, drives an unsteady flow through the cavity gaps. The time-averaged flowfield over the narrower gap resembles a pair of line vortices accompanied by a normal jet. Mass conservation requires that a much less intense flow develop over the larger gap. However, a lower limit to the small gap width was observed at which the mass flow through the small gap vanishes. An array of devices has been used in series with shear stress sensors for transition and turbulence control[3] and it has produced encouraging results. Saddoughi[8] is currently developing a larger springboard device to be used as a vortex generator for control of boundary layer separation.

These devices, although characterized by a single frequency, may be driven with amplitude-modulated signals at lower frequencies to which the global flow is receptive.[4] To use these devices to their full potential, it is vital that their behavior be fully understood. The devices must be accurately characterized to obtain a transfer function between the input (voltage) and output (mass ejection). To that end, it is necessary to consider the fluid-structural coupling of each actuator configuration. In this paper, the structural and fluid characteristics of the membrane actuator are investigated and a suitable model is considered. This model is then used in the analysis of experiments carried out with the actuator.

II. Theory and Modeling

To gain insight into the mechanisms that govern the fluid-structural coupling associated with the membrane actuator design, theoretical models are considered in this section. The analysis is separated into structural and fluids sections. For the structural analysis,

Received May 17, 1995; revision received Jan. 7, 1997; accepted for publication Jan. 26, 1997.

*Research Assistant, Department of Aeronautics and Astronautics.
†Associate Professor, Department of Aeronautics and Astronautics. Member AIAA.

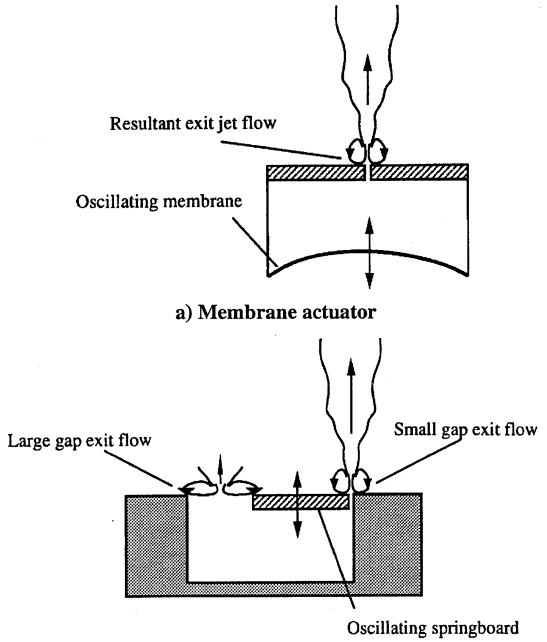

Fig. 1 Schematic cross-sectional views, showing the resulting time-averaged flowfields.

the device is modeled as a simple plate clamped at its edge. A transcendental equation is obtained and solved for the eigenvalues and eigenmodes of each configuration. In the fluids analysis, the device is simply modeled as a cavity filled with a compressible fluid that is forced out through one or more exits because of a pressure difference created by the action of the membrane, modeled as an oscillating piston. A set of coupled differential equations may then be written to describe the fluid properties both inside and outside the device.

A. Structural Modeling

The membrane device is modeled as a circular plate rigidly clamped at its edge. The solution to this problem is well documented,[9,10] and the first two natural frequencies are given by

$$\omega_{m1,2} = K_{1,2}\sqrt{\frac{4Et^3}{3(1-\nu_p^2)M_a D^4}} \tag{1}$$

where $K_{1,2} = 10.2$ and 21.3, respectively. The mode shapes are given by[9]

$$\Phi_{1,2} = \left\{ J_{0,1}\left(\frac{\sqrt{K_{1,2}}r}{D}\right) - \frac{J_{0,1}(\sqrt{K_{1,2}})}{I_{0,1}(\sqrt{K_{1,2}})} I_{0,1}\left(\frac{\sqrt{K_{1,2}}r}{D}\right)\right\}\cos(i\theta) \tag{2}$$

where J_n and I_n are the Bessel function and the modified Bessel function of the first kind of order n, respectively.

B. Fluid Modeling

Fluid effects arise when the flexible structure causes a compression of the fluid in the cavity and also when the unsteady flow that results from the unsteady cavity pressure develops through the orifice. The model used is illustrated in Fig. 2. The device is modeled as a piston of area A moving in a cylinder of height H. The piston displacement normalized by the cavity height x is equivalent to an average of the true membrane deflection described by Eq. (2). The piston resembles the membrane in that it causes an equivalent pressure change in the cavity. As the piston oscillates, the fluid in the cavity expands and compresses, leading to a fluctuating cavity pressure. Assuming the orifice area is large enough that viscous effects in the cavity may be ignored, the cavity pressure change drives a flow through the orifice at a uniform velocity, u. For smaller orifice diameters, viscous effects lead to a nonuniform velocity profile across the orifice and are discussed in Sec. II.D. The springboard

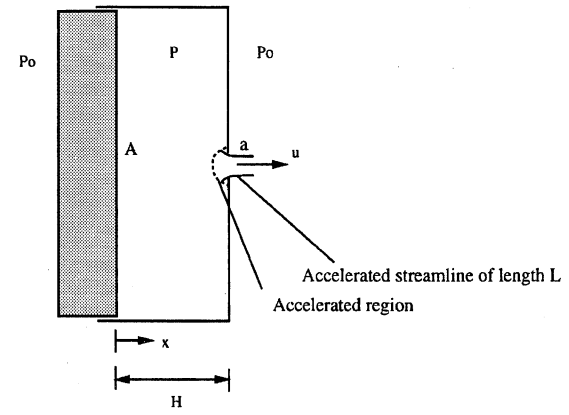

Fig. 2 Features of the model for analysis of fluid effects in a membrane actuator. The membrane is modeled as a piston of area A, that oscillates in a cavity from which flow is driven out through a small orifice of area a. The flow exit velocity u is assumed to be uniform and a nominal accelerating streamline, L, is assumed to stretch from a few diameters into the cavity to a few diameters into the emanating jet.

device may be modeled in an analogous manner with the exception that there are two exit gaps (one on either side of the cantilever).

The modeling leads to two coupled equations for the density of the fluid in the cavity and the jet velocity. The rate of change of density is simply given by the time derivative of the instantaneous mass in the cavity. By using the unsteady Bernoulli equation in streamline coordinates, the jet velocity may be written in terms of the pressure difference across the orifice and a nominal accelerating streamline length, L, typically a small multiple of the orifice diameter (here we assume $L = 2d$).

C. Coupled System

The result of combining structural and fluid effects may then be summarized below as a set of five, coupled, nonlinear first-order differential equations with states that include the membrane position and velocity (x_1 and x_2), the fluid density and pressure, and the jet velocity. The process is assumed to be isothermal. The forcing on the membrane is given by $G_0 \sin(\omega t)$, where G_0 may be calculated for the particular forcing method used:

$$\begin{aligned} \dot{x}_1 &= x_2 \\ M\dot{x}_2 &= -K_0 x_1 - C_0 x_2 - \frac{A}{H}(P - P_0) + \frac{G_0}{H}\sin(\omega t) \\ \dot{\rho} &= \frac{\rho(AH x_2 - ua)}{AH(1-x_1)} \qquad \dot{P} = RT\dot{\rho} \\ \dot{u} &= (P - P_0)/\rho L - u|u|/2L \end{aligned} \tag{3}$$

Equation (3) may be used as a transfer function to compute the actuator response. The structural stiffness and damping coefficients are dependent on the manufacturing technique and quality of the device and may be measured experimentally.

It is instructive to examine two limits for this system: 1) in which the cavity is sealed (i.e., $a \to 0$) and 2) in which the fluid is incompressible. In the first case, the terms associated with the jet vanish and the entire system may be written as a single differential equation for small values of x:

$$M\ddot{x} = -K_0 x - C_0\dot{x} - \frac{P_0 A x}{H(1-x)} + \frac{G_0}{H}\sin(\omega t) \tag{4}$$

Expanding the compressibility term reveals that, for small values of x, the undamped natural frequency is given by

$$\omega_0 = \sqrt{\frac{K_0 + P_0 A/H}{M}} \tag{5}$$

Thus, the effective stiffness increases as the ratio A/H. For larger values of x, quadratic and cubic nonlinearities will emerge, resulting in generation of harmonics and modulation of the fundamental

amplitude and a further shift in the natural frequency, proportional to x^2 (Ref. 11).

For the second case—that of an incompressible flow—the conservation of mass reduces to a simple relationship between the piston velocity and the jet velocity:

$$u = (AH/a)\dot{x} \tag{6}$$

This also results in a single differential equation for x:

$$\left(M + \rho_0 AL\frac{A}{a}\right)\ddot{x} = -K_0 x - C_0\dot{x} - \rho_0 AH\left(\frac{A}{a}\right)^2 \frac{\dot{x}\,|\dot{x}|}{2} + \frac{G_0}{H}\sin(\omega t) \tag{7}$$

Here the nonlinearities are more complex. On the left-hand side of Eq. (7), we see that there is an apparent mass term resulting from the unsteadiness of the fluid in the orifice. On the right-hand side, a term proportional to $\dot{x}|\dot{x}|(A/a)^2$ acts as a fluid damping term. It appears as a result of the energy loss associated with accelerating the fluid through the orifice. Note that as $a/A \to 0$, the term becomes singular because of infinite orifice velocities. In reality, the model is not valid in this limit because viscosity becomes dominant and restricts the mass flow through the hole. This is discussed in more detail in the following section. Expanding the $\dot{x}\,|\dot{x}|$ term in Fourier coefficients leads to linear and cubic damping terms, the second of which will result in a further source of frequency shift as the amplitude of the membrane oscillations increases. A full nonlinear perturbation analysis of this rich system is currently under way.

D. Effect of Viscosity

The preceding analysis on the fluid characteristics of the actuator was based on a uniform exit velocity u. As the orifice size decreases, the viscous layer in the orifice grows, leading to a restriction in the mass flow. Thus, at very small orifice sizes it is necessary to study the detail characteristics of the oscillating flow through the orifice. The orifice on a membrane device is circular, whereas the one on a large aspect ratio springboard device may be considered to be a two-dimensional slit.

This problem is similar to the Stokes oscillating plate problem, except that now the solid boundary is stationary and the flow adjacent to it is driven by a pressure gradient, $\Pi_x(t)$ (Ref. 12). Viscous effects lead to a boundary layer in the orifice whose thickness is governed by the viscosity and the frequency of oscillation and may be expressed in terms of a Stokes length scale, l_S. There is a radially independent, potential flow velocity component, $u_p(t) = u\cos(\omega t)$, associated with the pressure gradient and it is necessary to find a velocity, $u_v(r, t)$, such that $u_p + u_v$ satisfies the no-slip boundary condition. The simplest form for u_v is given by the diffusion equation.

The membrane problem is represented by an axisymmetric orifice and the diffusion equation in cylindrical coordinates is given by

$$\frac{\partial u_v}{\partial t} = \frac{\nu}{r}\frac{\partial}{\partial r}\left(r\frac{\partial u_v}{\partial r}\right) \tag{8}$$

Using the Stokes parameter $St_d = \sqrt{(\omega d^2/\nu)}$ and $\xi = 2r/d$, assuming a harmonic solution, $u_v(\xi, t) = \Re\{f(\xi)e^{i\omega t}\}$, and adding on the contribution from u_p, the solution for $u(\xi, t) = u(\xi, t)_v + u_p$ is given by

$$u(\xi, t) = \Re\left\{\frac{u\,[I_0(\sqrt{i}\,St_d\,\xi) - I_0(\sqrt{i}\,St_d)]}{[1 - I_0(\sqrt{i}\,St_d)]}\exp(i\omega t)\right\} \tag{9}$$

In the limit for small St_d, the flow is quasisteady and u may be shown to approximate the Hagen–Poiseuille formula

$$u(r, t) \approx (\Pi_x/4\mu)(d^2/4 - r^2) \tag{10}$$

When St_d is large, the instantaneous velocity profile is uniform except for a viscous layer close to the wall. As St_d decreases, this layer grows until it penetrates the entire flow region. As St_d decreases further the flow is choked—that is, the mass flow over half a cycle is reduced because of the effect of the viscous layer. Solving Eq. (9), the mass flow through the orifice of the membrane device is seen to fall by 95% at $St_d \approx 1.5$. The effective thickness of the Stokes layer is approximately $2.5\,l_S$, which corresponds to a critical Stokes parameter of 5.

Equation (9) describes the increase in the axial velocity as the Stokes parameter increases and the solution for large St_d tends toward an asymptote defined by inviscid flow. However, as the exit hole size increases (leading to an increase in St_d), mass conservation requires that the flow velocity should decrease proportionally to the hole area. Matching these two regimes will thus provide an optimum St_d at which the maximum flow velocity is achieved for a given device.

For small St_d, the axial velocity increases with d^2 or orifice area a [Eq. (10)]. When the boundary layer is restricted close to the orifice edge (at large St_d) so that the flow may be considered to be nearly inviscid, the axial velocity is then proportional to the membrane velocity and inversely proportional to a (from mass conservation). Matching the centerline velocities in these two regimes requires

$$\Pi_x a/4\pi\mu = (AH/a)\,\dot{x}$$

where $\Pi_x \approx P_0 x_0/t_c$. Assuming a harmonic solution for the membrane deflection and substituting the expression for the fundamental frequency from Eq. (1), one obtains, after some algebraic manipulation

$$a^2 = 4\pi^2\mu(Ct_cH/P_0) \tag{11}$$

giving

$$St_{\text{opt}} = 64\pi^2\left(\frac{\rho C^3 t_c H}{\nu P_0 A^2}\right)^{\frac{1}{4}} \tag{12}$$

where $C = K_1\sqrt{\{Et^3/[12(1 - \nu_p^2)M_a]\}}$, as defined by Eq. (1), and t_c is the orifice depth. St_{opt} is then the optimal Stokes parameter for a given actuator design. It depends on the variation of the natural frequency with the device dimensions, cavity volume, and depth of the orifice. St_{opt} for various actuator designs may be similarly computed if the natural frequency associated with the device is known.

III. Experimental Techniques and Data Reduction

To test the theory presented in the previous section, experiments were carried out in air with relatively large devices. These macro-sized devices were more easily fabricated and manipulated, allowing investigation of various configurations. Although much larger in size than would be practical for most flow control purposes, these devices provided a sufficient range of values of St_d for general conclusions to be drawn regarding their behavior with this parameter.

The device shown in Fig. 3 was made with a 170-μm-thick brass shim bonded at its edge to steel washers to act as the membrane. A small rectangular nickel-plated PZT-5H piezoceramic (250 μm thick) was bonded (using epoxy and silver paint) with one short edge rigidly fixed to the edge support. Because the purpose of the piezoceramic is to excite the membrane only at its resonant frequency, it may be small compared to the membrane size to minimize the interference on the motion of the membrane. In this case, it measured $D/8$ long and $D/20$ wide. A reinforced cap was mounted over the support washer, creating a 1.2-mm-deep closed cavity. The rigid cap in Fig. 3 consisted of a 1-mm-thick Plexiglas® annulus sandwiched with a 250-μm brass shim. The jet exit hole was drilled through this shim, permitting an orifice flow. Hole diameters varied from

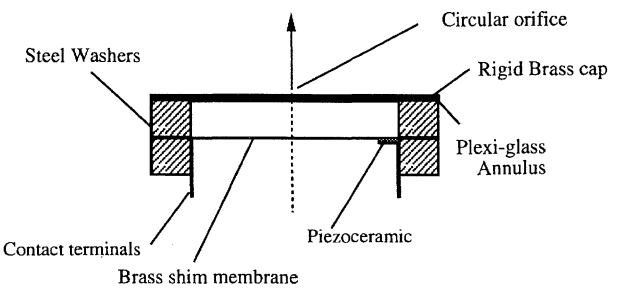

Fig. 3 Circular symmetric membrane actuator illustrated in cross section, showing the position of the piezoceramic and contact wires.

120 μm to 3.5 mm. Contact wires (24 gauge) were soldered onto the membrane and the ceramic.

To determine the structural characteristics of the actuators, an inductive sensor with a resolution of 5 μm was used to measure the deflection at the centroid of the membrane. Both actuator and sensor were held rigidly to a firm base to minimize structural vibrations. An amplified signal from a digital function generator was used to provide the input to the device. The dynamic response was measured with a sinusoidal sweep input about the resonant frequency of each device, which was obtained experimentally. The results were analyzed in terms of Bode plots. This procedure was carried out at different input voltages (from 5 to 90 V) to investigate amplitude characteristics and the linearity of the device response.

The jet characteristics of the device were investigated by using a constant temperature hot-wire anemometer to measure the axial velocity component in the jet. The hot-wire probe was traversed across the jet at different axial distances from the exit. Mean and fluctuating velocity measurements had an average error of ± 0.1 and ± 0.01 m/s, respectively.

To minimize structural differences that arise during fabrication of the actuators, the membrane diameter was kept constant at 25.4 mm, whereas the jet exit hole diameter was varied from 120 μm to 3.5 mm to obtain Stokes parameters of 2.4 to 30.

IV. Results and Discussion

The frequency of the fundamental mode computed by Eq. (1) agreed well with experimental data, with errors of <5%, indicating that the actuator behaves as a clamped circular plate and negligible interference was introduced by the piezoceramic. A typical Bode plot for the actuator with $St_d = 15.2$ (Fig. 4) shows an approximate second-order behavior with a 180-deg drop in phase and a 20-dB/decade rolloff in magnitude. Thus, the assumption of a second-order equation of motion [Eqs. (7) and (4)] is valid, at least to a first approximation, and nonlinearities are small and may be analyzed by perturbation theory.

The sharpness of the peak in the transfer function provides a measure of the damping in the system in terms of Q, the quality factor, and its position provides the fundamental mode precisely. The Q corresponding to Fig. 4 is 9 and indicates a lightly damped system (a nondimensional, linear second-order damping coefficient of 0.05).

The model described by Eq. (3) was solved by using a fourth-order Runge–Kutta algorithm (with a solution tolerance of 0.01%) and the results matched experimental data well, as shown in Fig. 5. The input was a burst of 100 periods at the fundamental frequency of 1750 Hz. By matching the rise and decay time of the membrane alone (that is, without the closed cavity), it was possible to extract the structural stiffness and damping coefficients (in this case the stiffness, $K_0 = 120 \times 10^6$ N/m, and the damping constant, $C_0 = 430$ Ns/m).

A. Nonlinear Characteristics

A plot of the transfer function at higher frequencies indicates the existence of a superharmonic mode at twice the frequency of the fundamental. Because no forcing was applied at the harmonic frequency, its magnitude was relatively small but it was seen to grow with the square of the input amplitude (not shown). Phase information was noisy and unreliable. Cleaner data may be obtained if the system is forced at a single frequency corresponding to its fundamental mode. A sweep input, no matter how slowly modulated, reduces the effective forcing at all frequencies. This has an effect on the absolute magnitude of the response but provides a true transfer function. Thus, linear and nonlinear system characteristics—namely, fundamental frequency and amplitude, harmonic frequency and amplitude, and damping and fundamental frequency shifts with input amplitude—may be extracted from a contour or surface plot of the transfer function plotted against frequency and input amplitude. Figure 6 is a series of such contour plots describing the behavior of the actuator with St_d and input amplitude. The contour line increments in each plot are identical.

When the cavity is fully sealed (Fig. 6a), the contour lines are closely spaced and there is a distinct increase in natural frequency with input amplitude and a modulation of the peak transfer function amplitude. This shift persists until an input amplitude of 50 V, above which the natural frequency remains constant. This behavior

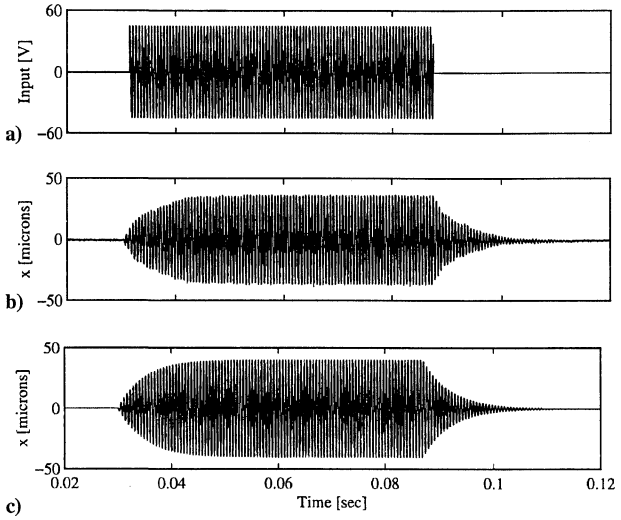

Fig. 5 a) Typical burst input across the piezoceramic that leads to b) a measured response that may be compared to c) numerical results for the actuator. Experimental data correspond to an actuator with $St_d = 15.2$, input amplitude = 20 V, and fundamental frequency = 1750 Hz.

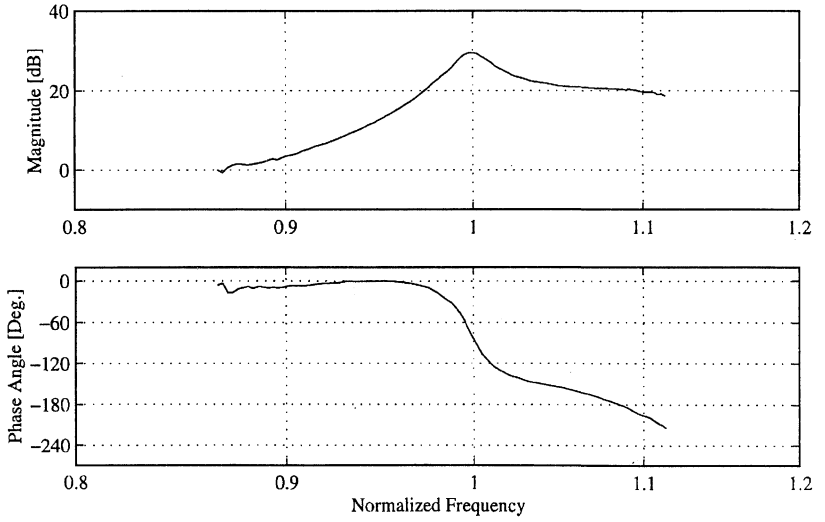

Fig. 4 Bode plot of a typical membrane actuator response: $St_d = 15.2$, input amplitude = 20 V, and fundamental frequency = 1750 Hz.

may be explained by considering the large fluid compression that introduces terms of order x^2 and x^3, which, from Eq. (4), lead to a quadratic amplitude modulation and a shift in natural frequency with input amplitude, respectively. As the input amplitude rises to a critical value, the membrane displacement reaches a maximum (saturation) and its response is unchanged for higher input amplitudes. The closely spaced contour lines indicate that the stiffness term dominates here and damping is relatively light and is mainly structural ($Q = 17$).

With a small exit hole (Fig. 6b) corresponding to a St_d of 3.5, the contour lines are spaced much farther apart and negligible frequency shift or amplitude modulation is observed. The transfer function peak amplitude is also smaller than that of the sealed case. This suggests that compressibility effects are negligible at the order of x^3. Furthermore, at this St_d the viscous layer penetrates the entire orifice area and reduces the mass flow through it so that nonlinear terms associated with the unsteady jet velocity are also small. The reduction in the peak amplitude of the transfer function comes about from the large added mass term similar to that in Eq. (7). The introduction of fluid damping through the orifice causes the increased separation between contour lines ($Q = 10$).

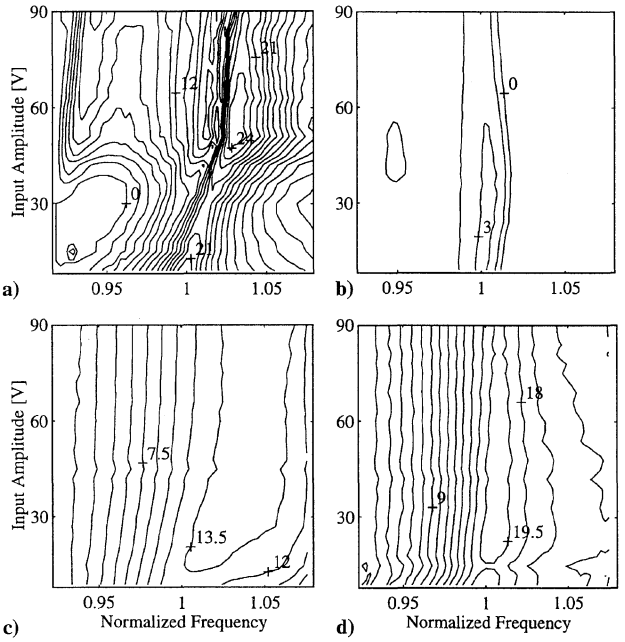

Fig. 6 Contours of the transfer function amplitude, in decibels, for various St_d: a) closed cavity (ω_0 = 1990 Hz), b) St_d = 3.5 (ω_0 = 2000 Hz), c) St_d = 9.8 (ω_0 = 1940 Hz), and d) St_d = 17.6 (ω_0 = 1950 Hz), where ω_0 is low-amplitude natural frequency. The transfer functions have been normalized for unity zero-frequency gain (0 dB) and contour line increments are identical for all plots.

As St_d increases (Fig. 6c), the contour lines move farther apart and a pronounced frequency shift develops. Now, the viscous layer in the orifice diminishes so that larger unsteady velocities develop that strengthen the damping term in Eq. (7) that lead to a relatively large natural frequency shift. Note that the term associated with the unsteady jet also introduces added linear damping, whose effect is readily observed by the increased separation between the contour lines in the vicinity of the fundamental frequency and the reduction in the low-amplitude fundamental frequency ($Q = 6$). As the input amplitude increases, the peak transfer function amplitude rapidly rises to a maximum and remains constant, indicating that the dominant effect at this Stokes parameter is that from the unsteady jet velocity.

At very large St_d (Fig. 6d), the contour lines are more closely spaced and no frequency shift or amplitude modulation is observed. The relatively large orifice size eliminates the effect of fluid nonlinearities and the flow may be considered to be effectively incompressible and inviscid. The shift in the natural frequency vanishes and the contour lines are more closely spaced, indicating that the reduced flow acceleration through the orifice decreases the fluid damping term ($Q = 9$). Furthermore, the peak transfer function amplitude remains constant.

Thus, the behavior of the actuator with St_d may be approximated by considering the limiting equations (7) and (4) individually. In reality, there is an intermediate range of St_d where both effects apply simultaneously and coupling terms may arise. Further nonlinear analysis is needed to obtain quantitative solutions in this range.

B. Jet Characteristics

Figure 7 illustrates the characteristics of the jet in terms of its mean and fluctuating centerline velocity and momentum thickness with respect to the nondimensional axial distance from the orifice, x/d. Figure 7a shows that the centerline velocity accelerates to a maximum at $x/d \approx 10$, after which there appears to exist a jet whose mean velocity varies as x^{-1}. This behavior is indicative of an axisymmetric jet. For $x/d < 10$, the jet is not fully developed and, as Fig. 7c indicates, consists of large fluctuations that correspond to the oscillating membrane. Figure 7b describes the extent of the shear layer with streamwise distance and shows an initially large region of influence, followed by a rapid reduction up to $x/d \approx 10$. The layer then grows linearly with x/d, again indicating the development of an axisymmetric jet. The results suggest that in the region close to the jet exit, a doughnut-shaped axisymmetric vortex structure surrounds the emanating jet, analogous to the longitudinal vortices observed by Jacobson and Reynolds.[3] This phenomenon is caused by the irreversible unsteady orifice flow and its influence extends to the point where a stable, well-developed jet can form. Figure 7c also shows the rapid decay of the fluctuating component with the streamwise distance, which begins only after the jet forms.

In Fig. 8a, the jet velocity profiles for $x/d > 10$ are plotted in similarity coordinates. It clearly shows that the jet is similar in the outer region. Figure 8b is a plot of the maximum centerline velocity, which occurs at the beginning of the similar jet, against St_d. The

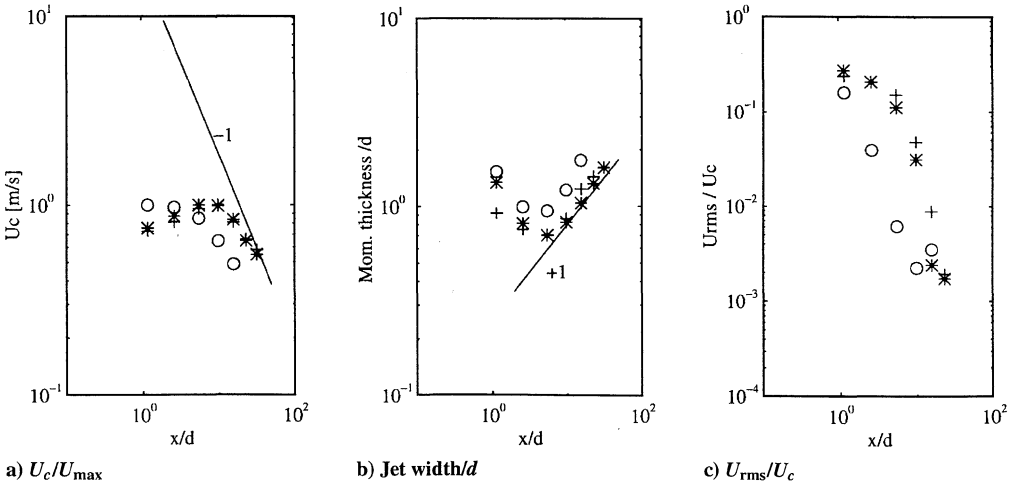

Fig. 7 Jet characteristics plotted against x/d. Symbols indicate input amplitude: ○, 30 V; ∗, 60 V; and +, 90 V. Solid lines indicate behavior of an axisymmetric jet.

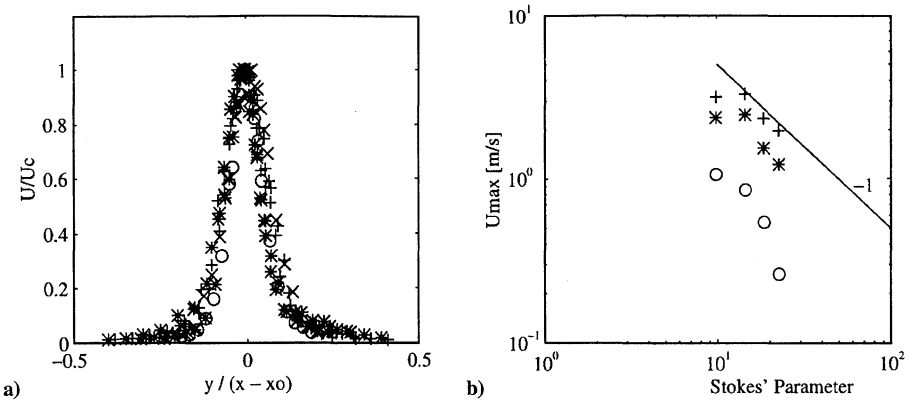

Fig. 8 a) Similarity profiles of the streamwise velocity component for $x/d > 10$ include profiles for different input voltages. b) U_{max} plotted against St_d for different forcing voltages (solid line with a slope of −1 indicates inviscid, incompressible theory). Symbols are as in Fig. 7.

plot indicates an optimum St_d of approximately 15, at which the actuator performs most efficiently (maximum $Re = 1.5 \times 10^2$). This compares well with the optimum value of 16 predicted by Eq. (12). Below this value, fluid nonlinearities are dominant, as discussed earlier, and above this value, the flow is essentially incompressible and inviscid (solid line) and the velocity falls with increasing orifice diameter. This critical St_d corresponds well with what was observed in Sec. IV.A as the point where the flow may be considered to be essentially incompressible and inviscid.

C. Comparisons of the Springboard and Membrane Actuators

As mentioned in preceding sections, both devices work on the same basic principle. The theoretical analysis discussed in Sec. II can be applied directly to the springboard device by a two-dimensional approach to represent a long, narrow exit slit instead of an axisymmetric one for the membrane device. A key difference between the two devices arises when viscous effects are taken into account. The springboard device has two gaps on either side of the cantilever for fluid flow out of the cavity, whereas the membrane device is restricted to having only one. Hence, when St_d gets small enough for viscous effects to cause significant resistance, the springboard device allows fluid to flow through the larger gap, effectively sealing the narrow gap. Compressibility effects become negligible and the mean velocity u is prevented from getting large enough for nonlinear fluid effects to be present unless both gaps correspond to low St_d. Similar experiments carried out with the springboard actuator show no natural frequency shift or superharmonic growth, except at large input amplitudes where the structural deflections become large enough to cause nonlinear effects. Furthermore, for St_d less than approximately 1.5, no jet flow could be detected over the narrow gap. It was also observed that the springboard jet velocities were on average higher than that for the membrane device. This is primarily due to the larger strokes attainable by the long and slender cantilever compared with the membrane, which was rigidly clamped around its entire edge. Hot-wire measurements were not made closer than 5 gap widths away from the exit, and errors in measuring the gap width could lead to errors of $\pm 10\%$ in St_d.

Taking into consideration the behavior of the actuators discussed here, an improved design could incorporate the benefits of both devices (that is, the nonintrusiveness of the membrane device and the larger stroke ability of the springboard device). A springboard mounted within a closed cavity with an exit hole would allow for a more compact, nonintrusive device. The springboard would be positioned so that the gaps between its edges and the cavity walls correspond to a low St_d, taking advantage of viscous sealing. The exit hole would be made to correspond to a higher St_d. Thus, fluid will enter and leave the cavity only through this exit hole.

V. Conclusions

A model for resonant fluid actuators that create an unsteady jet through the compression of a cavity was developed. It includes five coupled, nonlinear state equations. Compressibility and unsteadiness are shown to lead to nonlinear fluid effects that dominate when the jet exit hole is small. The model was compared to experimental data and successfully predicted trends in behavior of the membrane actuator. The Stokes parameter based on the jet exit diameter is used to describe the behavior of the device, and the results indicate that, for this particular actuator configuration, $St_d \approx 15$ defines an upper boundary for viscous effects above which the jet characteristics are governed by inviscid, incompressible theory. This critical value is accurately predicted by theory. It also defines the most efficient configuration for a given membrane actuator design. With this optimum configuration in mind, it is possible to make simple scaling arguments that allow the control resolution (that is, the jet size) to be maintained in different flow conditions.

A similar, axisymmetric jet is observed beyond 10 diameters away from the exit and sustains itself beyond 100 diameters. Close to the exit, the flow irreversibilities lead to a complex, vortical flow structure that could not be accurately investigated in this experiment.

Acknowledgments

This work was supported by Office of Naval Research Grant N00014-92-J-1918 monitored by L. Patrick Purtell. The authors would also like to acknowledge many fruitful discussions with John Dugundji, Jim Paduano, Stuart Jacobson, Errol Arkilic, and Olivier Piepsz.

References

[1]Choi, H., Moin, P., and Kim, J., "Active Turbulence Control for Drag Reduction in Wall-Bounded Flows," *Journal of Fluid Mechanics*, Vol. 262, March 1994, pp. 75–110.

[2]Gad-el-Hak, M., "Interactive Control of Turbulent Boundary Layers: A Futuristic Overview," AIAA Paper 93-3268, July 1993.

[3]Jacobson, S. A., and Reynolds, W. C., "An Experimental Investigation Towards the Active Control of Turbulent Boundary Layers," Thermosciences Div., Rept. TF-64, Dept. of Mechanical Engineering, Stanford Univ., Stanford, CA, March 1995.

[4]Wiltse, R. D., and Glezer, A., "Manipulation of Free Shear Flows Using Piezo Actuators," *Journal of Fluid Mechanics*, Vol. 249, April 1993, pp. 261–285.

[5]Gad-el-Hak, M., and Blackwelder, R. F., "Selective Suction for Controlling Bursting Events in a Boundary Layer," *AIAA Journal*, Vol. 27, No. 3, 1989, pp. 308–314.

[6]Coe, D. J., Allen, M. G., Trautman, M. A., and Glezer, A., "Micromachined Jets for Manipulation of Macro Flows," *Solid-State Sensor and Actuator Workshop*, Hilton Head, SC, 1994, pp. 243–247.

[7]James, R. D., Jacobs, J. W., and Glezer, A., "Experimental Investigation of a Turbulent Jet Produced by an Oscillating Surface Actuator," *Proceedings of the Twelfth US National Congress of Applied Mechanics*, Applied Mechanics Review, Seattle, WA, 1994, pp. S127–S131.

[8]Saddoughi, S. G., "Experimental Investigations of 'on-demand' Vortex Generators," *Annual Research Briefs*, Center for Turbulence Research, Stanford Univ./NASA Ames Research Center, Stanford, CA, 1994, pp. 197–203.

[9]Blevins, R. D., *Formulas for Natural Frequency and Mode Shape*, Krieger, Malabar, FL, 1984.

[10]Young, W. C., *Roark's Formulas for Stress & Strain*, 6th ed., McGraw–Hill, New York, 1989.

[11]Nayfeh, A. H., *Nonlinear Oscillations*, Wiley, New York, 1979.

[12]Sherman, F. S., *Viscous Flow*, McGraw–Hill, New York, 1968.

F. W. Chambers
Associate Editor